Computation of Transverse Optical Modes in Vertical-Cavity Surface-Emitting Lasers

Markus Daubenschüz

We present a finite-difference-based eigenvalue method for the computation of optical modes in waveguides with cylindrical symmetry. This approach is combined with the effective index method to determine the transverse modes in the resonator of vertical-cavity surface-emitting lasers (VCSELs) and to investigate the thermal guiding and the guiding provided by the buried oxide layers. We introduce the mathematical fundamentals of the finite difference method which is first applied to a step-index waveguide structure that allows a comparison with analytical solutions. Field distributions and polarizations of the modes are shown. Afterwards, multi-step and graded refractive index profiles as they arise in VCSELs are analyzed and the influence of the oxide width on the guiding is investigated.

1. Introduction

VCSELs are key optoelectronic devices for data communication in high-performance computing, data centers, and in-building networks [1, 2]. The performance of such lasers depends on numerous design parameters that influence the current flow, the heat generation inside the device, and the optical characteristics. To develop and optimize next-generation VCSELs with data rates of 28 Gbit/s and above [3, 4] or to enable new applications, an accurate prediction of the influence of design changes is inevitable. Therefore we have established a quasi-three-dimensional simulation framework to compute the electro-thermal characteristics of different epitaxial and geometrical designs [5, 6]. The simulations are based directly on the epitaxial design protocols. Beside the electrical and thermal characteristics, the knowledge of the optical properties is a major aspect. To complete our tool we have implemented a set of algorithms to compute the transverse modes inside the cavity. In Sect. 2 we show the mathematical foundation of the eigenvalue method based on finite differences and we compare the results with analytical solutions of step-index optical fiber structures. The next section extends the technique to VCSEL structures with rotational symmetry and a more complex refractive index profile.

2. Finite Difference Method

The implementation of the mode solver is based on the finite difference method (FDM). The underlying refractive index distribution is obtained by approximating the laser cavity by a longitudinally homogeneous waveguide structure. The mathematical approach of the FDM is the separation of electric and magnetic fields and the computation of

transverse fields by finite differences while analytical expressions are available in the direction of propagation. The generalized transmission line (GTL) equations derived from Maxwell's equations in cylindrical coordinates describe the relations between the electric and magnetic fields by [7]

$$-\mathrm{i}\epsilon_\mathrm{r}\begin{bmatrix} E_r \\ E_\phi \end{bmatrix} = \frac{\partial}{\partial\bar{z}}\begin{bmatrix} \bar{H}_\phi \\ -\bar{H}_r \end{bmatrix} + \begin{bmatrix} -\frac{1}{\bar{r}}\frac{\partial}{\partial\phi} \\ \frac{\partial}{\partial\bar{r}} \end{bmatrix}\bar{H}_z\,, \tag{1}$$

$$-\mathrm{i}\mu_\mathrm{r}\begin{bmatrix} \bar{H}_\phi \\ -\bar{H}_r \end{bmatrix} = \frac{\partial}{\partial\bar{z}}\begin{bmatrix} E_r \\ E_\phi \end{bmatrix} - \begin{bmatrix} \frac{\partial}{\partial\bar{r}} \\ \frac{1}{\bar{r}}\frac{\partial}{\partial\phi} \end{bmatrix}E_z\,, \tag{2}$$

where $\mathrm{i}=\sqrt{-1}$ and ϵ_r and μ_r are the relative permittivity and permeability, respectively. We have normalized the coordinates $u=r,z$ with the free-space wavenumber $k=2\pi/\lambda$ as $\bar{u}=uk$ and the magnetic field $\bar{H}=HZ_0$ with the free-space wave impedance $Z_0=\sqrt{\mu_0/\epsilon_0}$. Applying Faraday's law

$$\bar{H}_z = \mathrm{i}\frac{1}{\mu_\mathrm{r}\bar{r}}\begin{bmatrix} -\frac{1}{\bar{r}}\frac{\partial}{\partial\phi} & \frac{\partial}{\partial\bar{r}}\bar{r} \end{bmatrix}\begin{bmatrix} \bar{r}E_r \\ E_\phi \end{bmatrix} \tag{3}$$

in (1) and Ampère's law for dielectric material

$$E_z = -\mathrm{i}\frac{1}{\epsilon_\mathrm{r}\bar{r}}\begin{bmatrix} \frac{\partial}{\partial\bar{r}} & \frac{\partial}{\partial\phi} \end{bmatrix}\begin{bmatrix} \bar{r}\bar{H}_\phi \\ -\bar{H}_r \end{bmatrix} \tag{4}$$

in (2), the GTL equations are rewritten as

$$\frac{\partial[H]_\mathrm{t}}{\partial\bar{z}} = -\mathrm{i}\mathbf{R}_\mathrm{E}[E]_\mathrm{t}\,, \qquad \frac{\partial[E]_\mathrm{t}}{\partial\bar{z}} = -\mathrm{i}\mathbf{R}_\mathrm{H}[H]_\mathrm{t} \tag{5}$$

with the transverse field components

$$[E]_\mathrm{t} = \begin{bmatrix} \bar{r}E_r \\ E_\phi \end{bmatrix}, \qquad [H]_\mathrm{t} = \begin{bmatrix} \bar{r}\bar{H}_\phi \\ -\bar{H}_r \end{bmatrix}. \tag{6}$$

The matrix elements $\mathbf{R}_\mathrm{E}$ and $\mathbf{R}_\mathrm{H}$ in (5) include the derivatives in $\bar{r}$- and ϕ-directions and the material parameters ϵ_r and μ_r of the structure. The two matrices have the form [8]

$$\mathbf{R}_\mathrm{E} = \begin{bmatrix} \epsilon_\mathrm{r} + \frac{1}{\bar{r}^2}\frac{\partial}{\partial\phi}\frac{1}{\mu_\mathrm{r}}\frac{\partial}{\partial\phi} & -\frac{1}{\bar{r}}\frac{\partial}{\partial\phi}\frac{1}{\mu_\mathrm{r}}\frac{\partial}{\partial\bar{r}}\bar{r} \\ -\frac{\partial}{\partial\bar{r}}\frac{1}{\mu_\mathrm{r}\bar{r}^2}\frac{\partial}{\partial\phi} & \epsilon_\mathrm{r} + \frac{\partial}{\partial\bar{r}}\frac{1}{\mu_\mathrm{r}\bar{r}}\frac{\partial}{\partial\bar{r}}\bar{r} \end{bmatrix} \tag{7}$$

and

$$\mathbf{R}_\mathrm{H} = \begin{bmatrix} \mu_\mathrm{r} + \bar{r}\frac{\partial}{\partial\bar{r}}\frac{1}{\epsilon_\mathrm{r}\bar{r}}\frac{\partial}{\partial\bar{r}} & \bar{r}\frac{\partial}{\partial\bar{r}}\frac{1}{\epsilon_\mathrm{r}\bar{r}}\frac{\partial}{\partial\phi} \\ \frac{1}{\bar{r}^2}\frac{\partial}{\partial\phi}\frac{1}{\epsilon_\mathrm{r}}\frac{\partial}{\partial\bar{r}} & \mu_\mathrm{r} + \frac{1}{\bar{r}^2}\frac{\partial}{\partial\phi}\frac{1}{\epsilon_\mathrm{r}}\frac{\partial}{\partial\phi} \end{bmatrix}. \tag{8}$$

The combination of the two equations in (5) leads to

$$\frac{\partial^2[E]_\mathrm{t}}{\partial\bar{z}^2} - \mathbf{Q}_\mathrm{E}[E]_\mathrm{t} = 0\,, \tag{9}$$

$$\frac{\partial^2 [H]_\mathrm{t}}{\partial \bar{z}^2} - \mathbf{Q}_\mathrm{H} [H]_\mathrm{t} = 0\,, \tag{10}$$

where we used the operation matrices $\mathbf{Q}_\mathrm{E}$ and $\mathbf{Q}_\mathrm{H}$ that arise from the matrix products

$$\mathbf{Q}_\mathrm{E} = -\mathbf{R}_\mathrm{H}\mathbf{R}_\mathrm{E}\,, \qquad\qquad \mathbf{Q}_\mathrm{H} = -\mathbf{R}_\mathrm{E}\mathbf{R}_\mathrm{H}\,. \tag{11}$$

Only the transverse field components are included in (9) and (10) and the derivatives in longitudinal $\bar{z}$ and transverse ϕ- and $\bar{r}$-directions are separated. By replacing the derivatives in (7) and (8) by finite differences one can solve the system of equations by a transformation to principal axes

$$\mathbf{T}_\mathrm{E}\mathbf{\Gamma}_\mathrm{E}^2\mathbf{T}_\mathrm{E}^{-1} = \mathbf{Q}_\mathrm{E}\,, \qquad\qquad \mathbf{T}_\mathrm{H}\mathbf{\Gamma}_\mathrm{H}^2\mathbf{T}_\mathrm{H}^{-1} = \mathbf{Q}_\mathrm{H}\,, \tag{12}$$

where the matrices $\mathbf{\Gamma}_\mathrm{E,H}$ include the eigenvalues and the matrices $\mathbf{T}_\mathrm{E,H}$ the eigenvectors of the $\mathbf{Q}_\mathrm{E,H}$ matrices. The columns of eigenvectors correspond to the field distributions of the modes in the structure, whereas the principal axis of the eigenvalues Γ contains the propagation constants of the modes in the form

$$\bar{\gamma} = \sqrt{\Gamma} = \bar{\kappa} + \mathrm{i}\bar{n}_\mathrm{eff}\,, \tag{13}$$

where $\bar{\kappa} = \alpha/(2k)$ is the amplitude attenuation coefficient normalized with k and $\bar{n}_\mathrm{eff}$ is the effective index such that the mode propagates with the propagation factor $\exp\{-\bar{\gamma}\bar{z}\} = \exp\{-\alpha z/2\}\exp\{-\mathrm{i}\bar{n}_\mathrm{eff}kz\}$ for a wave traveling in $+z$-direction. We assume structures with material parameters not depending on the ϕ-direction and a perfect cylindrical symmetry. One can then replace the ϕ-dependency with

$$E_r, \bar{H}_\phi \propto \cos(m\phi)\,, \qquad\qquad E_\phi, \bar{H}_r \propto \sin(m\phi) \tag{14}$$

or vice versa. Therefore we can simplify (7) and (8) to the forms

$$\mathbf{R}_\mathrm{E} = \begin{bmatrix} \epsilon_\mathrm{r} - m^2\frac{1}{\mu_\mathrm{r}\bar{r}^2} & -m\frac{1}{\mu_\mathrm{r}}D_{\bar{r}}\bar{r} \\ mD_{\bar{r}}\frac{1}{\mu_\mathrm{r}\bar{r}^2} & \epsilon_\mathrm{r} + D_{\bar{r}}\frac{1}{\mu_\mathrm{r}\bar{r}}D_{\bar{r}}\bar{r} \end{bmatrix}, \tag{15}$$

$$\mathbf{R}_\mathrm{H} = \begin{bmatrix} \mu_\mathrm{r} + \bar{r}D_{\bar{r}}\frac{1}{\epsilon_\mathrm{r}\bar{r}}D_{\bar{r}} & m\bar{r}D_{\bar{r}}\frac{1}{\epsilon_\mathrm{r}\bar{r}} \\ -m\frac{1}{\epsilon_\mathrm{r}\bar{r}^2}D_{\bar{r}} & \mu_\mathrm{r} - m^2\frac{1}{\epsilon_\mathrm{r}\bar{r}^2} \end{bmatrix}, \tag{16}$$

where we have substituted the derivative $\frac{\partial}{\partial\bar{r}}$ by a finite difference matrix $D_{\bar{r}}$ [7]. The related coordinate system for the discretization with finite differences is shown in Fig. 1. Worth to mention is the half-step shift $\Delta\bar{r}/2$ between the $E_r, \bar{H}_\phi$ and $E_\phi, \bar{H}_r$ fields, which is caused by the first-order derivative of the coupling between the field components in (15) and (16). As boundary conditions in the center at $\bar{r} = 0$ we use the Neumann condition $\frac{\partial F}{\partial\bar{r}} = 0$ for $E_\phi, \bar{H}_r$ and the Dirichlet condition $F = 0$ for $\bar{r}E_r, \bar{r}\bar{H}_\phi$. Due to the multiplication of E_r and $\bar{H}_\phi$ with $\bar{r}$ the Dirichlet boundary condition is fulfilled without forcing the field component itself to zero.

The results of the finite difference computation are compared to an analytical solution for a weakly guiding step-index fiber with a refractive index $\bar{n}_\mathrm{co} = 1.5$ in the core with

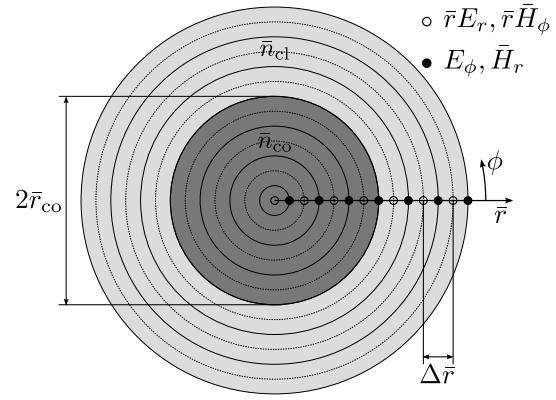

Fig. 1: Coordinate system for a finite difference discretization of a step-index fiber with rotational symmetry.

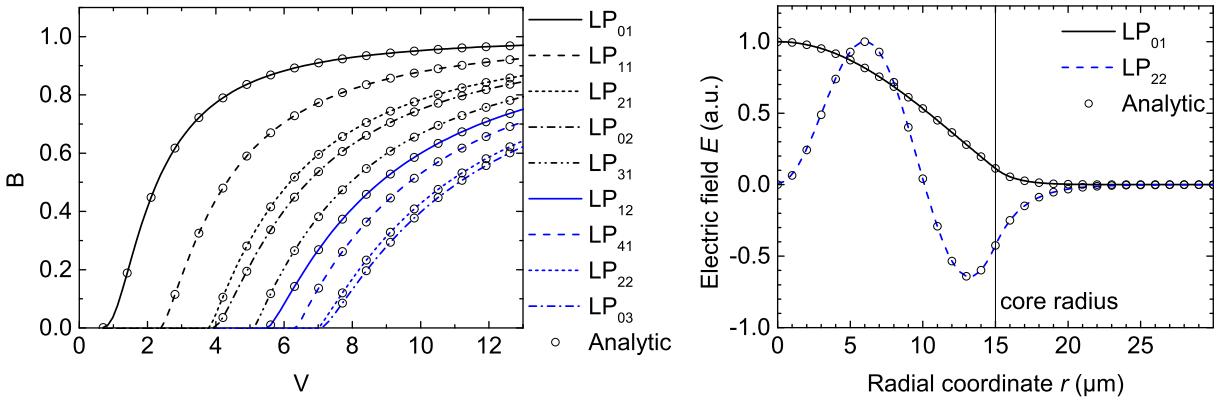

Fig. 2: Comparison of analytic and finite difference solutions of the phase parameter $B = (\bar{n}_{\mathrm{eff}}^2 - \bar{n}_{\mathrm{cl}}^2)/(\bar{n}_{\mathrm{co}}^2 - \bar{n}_{\mathrm{cl}}^2)$ and the frequency parameter $V = kr_{\mathrm{co}}\sqrt{\bar{n}_{\mathrm{co}}^2 - \bar{n}_{\mathrm{cl}}^2}$ for the first nine LP modes of a step-index fiber (left) and two radial field distributions for refractive indices $\bar{n}_{\mathrm{co}} = 1.5$ and $\bar{n}_{\mathrm{cl}} = 1.497$ and a core radius $r_{\mathrm{co}} = 15\,\mu\mathrm{m}$ (right). The radius of the simulation window is $80\,\mu\mathrm{m}$ and the discretization step width is $0.1\,\mu\mathrm{m}$

.

$0 \le r \le \bar{r}_{\mathrm{co}}\lambda/(2\pi)$ and $\bar{n}_{\mathrm{cl}} = 1.497$ in the cladding with $r > \bar{r}_{\mathrm{co}}\lambda/(2\pi)$. The analytical solutions are found by solving the characteristic equation [9, 10]

$$\frac{u \cdot J_l(u)}{J_{l-1}(u)} = -\frac{w \cdot K_l(w)}{K_{l-1}(w)} \tag{17}$$

with the Bessel function J describing the field distribution in the core and the modified Hankel function K for the evanescent fields in the cladding. Solutions of the FDM are the so-called EH and HE modes. It is convenient to approximate the modes inside a VCSEL as a superposition of nearly degenerated EH and HE modes. These are the linearly polarized LP_{lp} modes in the combination $\mathrm{EH}_{l-1,p}$ and $\mathrm{HE}_{l+1,p}$ with the azimuthal order l and the radial order p [9]. In Fig. 2 (left) we plot the BV diagram of the fiber for the first nine LP modes. There is a perfect accordance of analytic and finite difference solutions. The radial field distributions of two modes in the same fiber with core radius $r_{\mathrm{co}} = 15\,\mu\mathrm{m}$ are shown in Fig. 2 (right). To illustrate the origin of the LP modes we show in Fig. 3 the two-dimensional electric field profiles and the corresponding electric field polarizations of two quasi-degenerated EH_{01} and HE_{21} modes with an effective index $\bar{n}_{\mathrm{eff}} = 1.4997$ for

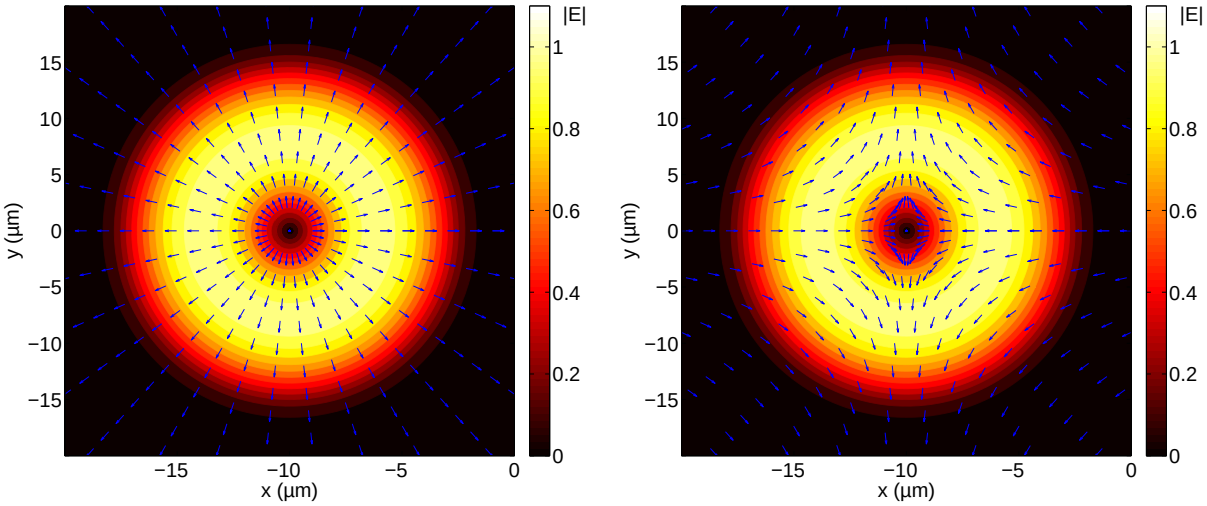

Fig. 3: Two-dimensional electric field profiles and electric field polarizations of the EH_{01} (left) and HE_{21} (right) modes in a step-index fiber with $\bar{n}_{co} = 1.5$, $\bar{n}_{cl} = 1.497$, and $r_{co} = 15\,\mu m$.

$r_{co} = 15\,\mu m$. The addition of these modes forms the linearly polarized LP_{11} mode that is shown in Fig. 4. It should be mentioned that this mode can occur in two orientations, namely $\sin\phi$ and $\cos\phi$, and two orthogonal linear polarizations.

3. VCSEL Modes

The FDM described in the previous section enables us to evaluate the influence of different design parameters on the optical guiding in VCSEL structures with more complex refractive index profiles compared to a simple step-index fiber. To determine the radial refractive index profile we combine our approach with the effective index method [11] that

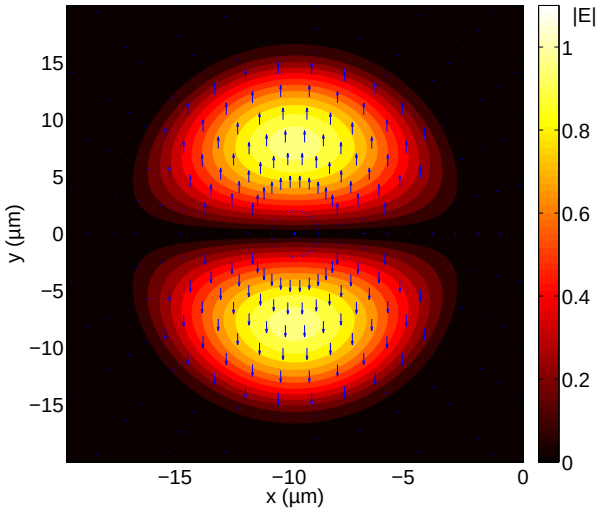

Fig. 4: Two-dimensional electric field profile and electric field polarization of the LP_{11} mode that originates from the addition of the EH_{01} and HE_{21} modes in Fig. 3.

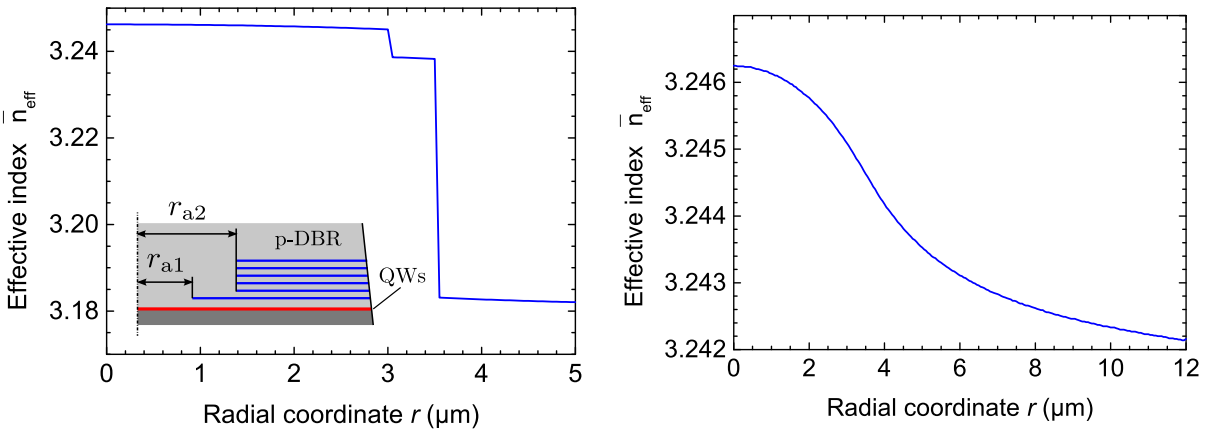

Fig. 5: Radial effective index profile of an oxide-confined VCSEL with one main aperture with active radius $r_{a1} = 3\,\mu\mathrm{m}$ and five additional apertures with $r_{a2} = 3.5\,\mu\mathrm{m}$ as well as a thermally induced index profile (left) and the same profile without the influence of the oxide layers (right).

gives a relation between the change of the resonance wavelength $\Delta\lambda$ and the change of the effective index $\Delta\bar{n}_{\mathrm{eff}}$, namely

$$\frac{\Delta\lambda}{\lambda} = \frac{\Delta\bar{n}_{\mathrm{eff}}}{\bar{n}_{\mathrm{eff}}} \tag{18}$$

with the initial resonance wavelength λ and the effective index $\bar{n}_{\mathrm{eff}}$. The values of $\Delta\lambda = \Delta\lambda(r)$ are determined with the one-dimensional transfer matrix method [12]. With this approximation we can evaluate the influence of thermal lensing as well as the guiding provided by one or multiple oxide layers. Figure 5 (left) depicts the effective index profile of an oxide-confined datacom VCSEL with one main aperture and five additional apertures with larger diameter to reduce the capacitance of the device, as indicated in the inset. The radii are $r_{a1} = 3\,\mu\mathrm{m}$ and $r_{a2} = 3.5\,\mu\mathrm{m}$ for the main and the additional apertures, respectively. The laser cavity consists of three quantum wells sandwiched between 26 top and 33.5 bottom mirror pairs. The influence of the oxide layers on the effective index profile is quite strong, which is due to the high index difference $\Delta\bar{n} \approx 1.4$ between aluminum oxide and AlGaAs. The effective index steps are $\Delta\bar{n}_{\mathrm{eff}} = 0.006$ and 0.055 for the main and the additional apertures, respectively. The profile in Fig. 5 (left) includes both the oxide and thermal effects on the refractive index. In contrast, Fig. 5 (right) exclusively shows the thermally induced effective index profile for a dissipated electrical power $P_{\mathrm{diss}} = 14\,\mathrm{mW}$. The radial temperature profile inside the cavity causes a decreasing $\bar{n}_{\mathrm{eff}}$ with increasing radial coordinate. This $\bar{n}_{\mathrm{eff}}$ profile results in the so-called thermal lensing, which in the given case is small compared to the built-in guiding. The LP modes guided by the effective index profile $\bar{n}_{\mathrm{eff}}(r)$ are then computed according to Sect. 2. The first six transverse modes of the oxide configuration of Fig. 5 (left) are displayed in Fig. 6 (left). On the right side of Fig. 6 we set the radii r_{a2} of the additional oxide layers to 3, 3.5, and 4 µm and compute the profiles of the corresponding fundamental LP_{01} modes. Larger r_{a2} obvious lead to a widening of the mode profiles. This effect is expected to saturate owing to the guiding effect of $\Delta\bar{n}_{\mathrm{eff}}$ at $r = r_{a1}$.

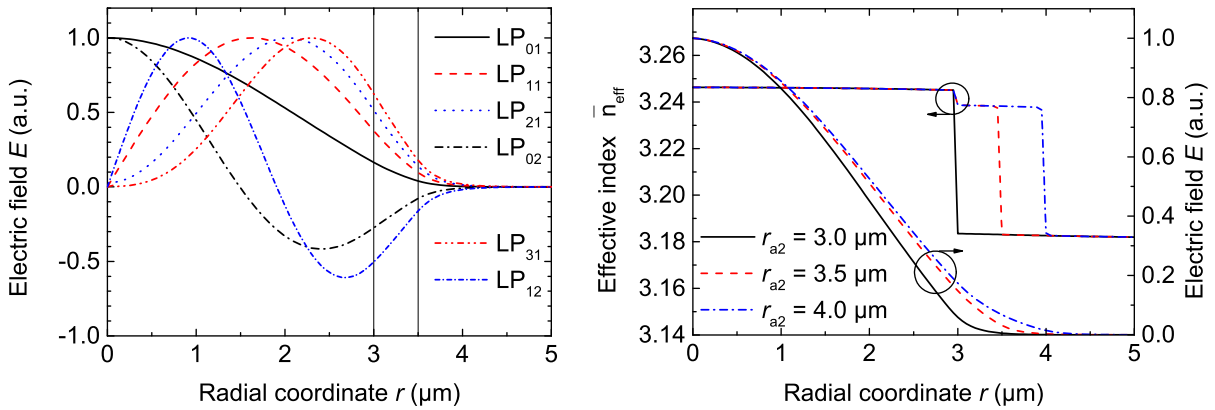

Fig. 6: Radial field profiles of the first six transverse modes in an oxide-confined VCSEL cavity with $r_{a1} = 3\,\mu m$ and $r_{a2} = 3.5\,\mu m$ (indicated as vertical lines) (left) and the resulting LP_{01} modes of the same structure with changing r_{a2} (right).

4. Conclusion

We have introduced a finite-difference-based eigenvalue method for the computation of optical modes in cylindrical geometries. In combination with the effective index method this approach can be used to evaluate the distributions of the linearly polarized LP modes inside the cavity of VCSELs with complex refractive index profiles. As a brief example we have calculated different modes of an oxide-confined VCSEL and have investigated the influence of variations of an oxide aperture diameter on the optical guiding.

Acknowledgment

We thank Philips Technologie GmbH, U-L-M Photonics, Germany for the fruitful collaboration and the German Federal Ministry of Education and Research (BMBF) for funding the HyPOT project.

References

[1] K. Jackson and C. Schow, "VCSEL-Based Transceiver for Data Communication", Chap. 14 in *VCSELs*, R. Michalzik (Ed.), pp. 431–448, Berlin: Springer, 2013.

[2] D. Kuchta, "Progress in VCSEL-Based Parallel Links", Chap. 16 in *VCSELs*, R. Michalzik (Ed.), pp. 473–519, Berlin: Springer, 2013.

[3] P. Westbergh, R. Safaisini, E. Haglund, J. Gustavsson, A. Larsson, M. Green, R. Lawrence, and A. Joel, "High-speed oxide confined 850 nm VCSELs operating error-free at 40 Gb/s up to 85°C", *IEEE Photon. Technol. Lett.*, vol. 25, pp. 768–771, 2013.

[4] D.M. Kuchta, A.V. Rylyakov, F.E. Doany, C.L. Schow, J.E. Proesel, C.W. Baks, P. Westbergh, J.S. Gustavsson, and A. Larsson, "A 71-Gb/s NRZ modulated 850-nm VCSEL-based optical link", *IEEE Photon. Technol. Lett.*, vol. 27, pp. 577–580, 2015.

[5] M. Daubenschüz, P. Gerlach, and R. Michalzik, "Electro-thermal characteristics of VCSELs: simulations and experiments", in *Semiconductor Lasers and Laser Dynamics VI*, K.P. Panajotov, M. Sciamanna, A.A. Valle, R. Michalzik (Eds.), Proc. SPIE 9134, pp. 91342H-1–8, 2014.

[6] M. Daubenschüz, P. Gerlach, and R. Michalzik, "Epitaxy-based electro-thermal simulation approach for vertical-cavity surface-emitting laser structures", in Online Digest *Conf. on Lasers and Electro-Optics Europe, CLEO/Europe 2015*, paper CB-P.14, one page. Munich, Germany, Jun. 2015.

[7] R. Pregla, *Analysis of Electromagnetic Fields and Waves*, Weilheim: Wiley, 2013.

[8] S.T. Helfert,"Modelling the coupling of electromagnetic waves to cylindrical waveguides with the method of lines", *Opt. Quantum Electron.*, vol. 48, pp. 242-1–14, 2016.

[9] H.-G. Unger, *Optische Nachrichtentechnik* (2nd ed.), Heidelberg: Hüthig, 1990.

[10] K. Okamoto, *Fundamental of Optical Waveguides*, San Diego: Academic Press, 2000.

[11] G.R. Hadley, "Effective index model for vertical-cavity surface-emitting lasers", *Opt. Lett.*, vol. 20, pp. 1483–1485, 1995.

[12] R. Michalzik, "VCSEL-Fundamentals", Chap. 2 in *VCSELs*, R. Michalzik (Ed.), pp. 19–75, Berlin: Springer, 2013.